Interstitial nitrogen atoms in diamond. A quantum mechanical investigation of its electronic and vibrational properties

Simone Salustro*[,a], Fabien Pascale[b], William C. Mackrodt[a], Corentin Ravoux[a,c], Alessandro Erba[a], Roberto Dovesi[a]

[a]Dipartimento di Chimica, Università di Torino, via Giuria 5, IT-10125 Torino, Italy.
[b]Université de Lorraine – Nancy, CNRS, Laboratoire de Physique et Chimie Théoriques, UMR 7019, Vandœuvre-lès-Nancy, 54506, France
[c]Laboratoire Structure Propriétés et Modélisation des Solides (SPMS), CentraleSupélec, Bâtiment G. EIFFEL, 3 rue Joliot Curie, 91190 GIF-SUR-YVETTE, France

*Corresponding author: Simone Salustro E-mail: simone.salustro@gmail.com

Abstract

The electronic and vibrational features of the single- (I_{1N}) and double- (I_{2N}) nitrogen interstitial defects in diamond are investigated at the quantum mechanical level using a periodic supercell approach based on hybrid functionals constructed from all electron Gaussian basis sets within the CRYSTAL code. The results are compared with those of the well characterized ⟨100⟩ split self-interstitial defect (I_{2C}). The effect of defect concentration has been investigated using supercells with different size, containing 64 and 216 atoms. Band structure, formation energy, charge and spin density distributions of each defect are analyzed. Irrespective of the defect concentration, these defects show important features for both IR and Raman spectroscopies. Stretching modes of the two atoms involved in the defect are calculated to be around 1837, 1761 and 1897 cm^{-1} for the I_{1N}, I_{2N} and I_{2C} case, respectively. Since they are well removed from the one-phonon mode of pristine diamond (1332 cm^{-1}), they are, in principle, detectable from the experimental point of view.

1 Introduction

Natural and synthetic diamonds are characterized by a large variety of point-defects, including vacancies, interstitials, substitutionals and combinations of them. These strongly affect the exceptional properties (high Young's modulus and thermal conductivity, broad transparency range, high carrier mobility, *etc.*) of the ideal defect-free crystalline structure.[1–4] The investigation of native and radiation-induced point-defects in diamond (as well as in other semiconductors) has thus attracted extensive theoretical and experimental interest.[1–30]Despite the simplicity of the perfect diamond lattice, a wealth of different defects can be formed, whose electronic structures and spectroscopic fingerprints remain to be characterised in any detail at the atomic level.

A key feature of radiation-damaged diamonds is associated with the relative abundance of sp^3 and graphitic-like sp^2 carbon atoms. In this respect, given the specific spectroscopic fingerprint of different

hybridizations of carbon atoms,[10,11] Infrared (IR) and Raman spectroscopies represent ideal experimental techniques with which to characterize the atomic nature of the various point-defects in both diamond and diamond-like materials.[12–21] In this regard, in a series of previous publications[25–30] some of the present authors have proposed the quantum-mechanical characterization of several point-defects in diamond, including the simulation of vibrational IR and Raman spectra.

Since first principles techniques have become available, both finite cluster and periodic supercell approaches have been used,[23,24] mainly based on the simplest formulation of Density Functional Theory (DFT), notably the Local Density and Generalized Gradient Approximations (LDA and GGA, respectively). However, these are known to poorly describe the exchange interactions of well-localized unpaired electrons and to underestimate substantially the lowest energy band-gaps, where defect states are located.

Theoretical simulations of IR and Raman spectra of extended solids have recently become feasible at the quantum-mechanical level of theory, so that computational spectroscopy can now be an effective complementary tool in the interpretation of experimental spectra, and an essential means to the atomic characterization of their features.[31–37]

In this work, the analysis of the 〈100〉 split self-interstitial[38] is extended to cases in which one or both the atoms forming the defect are nitrogen atoms.

In 2004, Goss *et al.*[39] reported a quantum mechanical investigation of both the electronic and vibrational properties of several interstitial nitrogen defects, including those considered in the present paper. In this study,[39]the defective structure was modelled on periodic supercells, and based a local spin density functional[40] and norm-conserving pseudopotentials for the core electrons, in the calculation of the electronic wavefunctions. By contrast, the electronic and vibrational properties reported here are derived from all electron Gaussian orbital B3LYP[41,42] calculations, again based on periodic supercells, as embodied in the CRYSTAL code. As outlined previously,[43–48] the B3LYP hybrid functional, with 20% non-local exact exchange, leads to a proper description of (electronic) spin polarisation, while the use of (periodic) supercells allows the effects of defect concentration to be explored.

The paper is structured as follows. Section 2 contains the details of the computational procedures and conditions. Section 3 is organised in two parts: Section 3.1 describes the fully-relaxed structures of the defective lattices, their charge (and spin) distributions and band structures; Section 3.2 reports the corresponding vibrational features and their detailed analysis. Section 4 contains the discussion and Section 5 contains the conclusions of this study.

2 Computational methods

Prior to the main body of investigations using the global B3LYP functional, preliminary calculations for selected electronic and energetic features were performed using other DFT formulations, ranging from pure (LDA[40] and PBE[49]), to global hybrid (PBE0[50]), and range-separated hybrid (HSE06[51]). Pople's standard 6-21G[52] all electron basis sets of Gaussian functions have been adopted for both carbon and nitrogen, except for values of 0.228 $Bohr^{-2}$ and 0.30 $Bohr^{-2}$ for the outermost sp orbitals of the host and dopant atoms respectively. As elsewhere,[25–30] the five parameters, T_i, that control the truncation of the infinite Coulomb and exchange series[37] were set to 10^{-8} (T_1–T_4) and 10^{-16} for T_5, while the Self-Consistent Field (SCF) convergence threshold for the energy was set to 10^{-10} hartree for vibration frequency calculations.

In the CRYSTAL code,[37] the DFT exchange–correlation contribution and its gradient are evaluated by numerical integration over the unit cell volume, where the generation of the integration grid points is based

on an atomic partition method, originally developed by Becke[53] for molecules and extended further to periodic systems. Within this scheme the unit cell is partitioned into atomic volumes centered on the nuclei, where each point has an associated weight. Radial and angular points for the integration grid are generated by Gauss–Legendre quadrature and Lebedev two-dimensional distributions respectively. The choice of a suitable grid is crucial both for numerical accuracy and the optimisation of computational resources. In this study a default[54] pruned grid with 75 radial and 974 angular points has been used, whose accuracy can be measured by comparing the integrated charge density of N_i = 1304.016 for the largest supercell here considered (216 + 1 atoms), with the total number of 1304 electrons in the unit cell.

As in previous studies,[25–30] a periodic supercell approach has been used to simulate different defect concentrations. In this work two cubic supercells have been considered, containing respectively 64 + 1 (S_{64}) and 216 + 1 (S_{216}) atoms. For each cell a different Γ-centered Pack–Monkhorst[55] grid for sampling the reciprocal space has been used, consisting of 4 × 4 × 4 = 64 (S_{64}) and 2 × 2 × 2 = 8 (S_{216}) k-points in the first Brillouin zone.

Harmonic phonon frequencies (*i.e.* wavenumbers), ω_p, at the Γ point (the center of the first Brillouin zone in reciprocal space) were obtained from the diagonalization of the mass-weighted Hessian matrix of the second energy derivatives with respect to atomic displacements u:[34,56–59]

$$W^{i'}_{ai,bj} = \frac{H^{0}_{ai,bj}}{\sqrt{M_a M_b}} \quad \text{with} \quad H^{0}_{ai,bj} = \left(\frac{\partial^2 E}{\partial u^{0}_{ai} \partial u^{0}_{bj}} \right), \tag{1}$$

where atoms a and b (with atomic masses M_a and M_b) in the reference cell, 0, are displaced along the i-th and j-th Cartesian directions, respectively. The Raman intensity of the Stokes line of a phonon mode Q_p, characterized by a frequency ω_p, active due to the $\alpha_{ii'}$ component of the polarizability tensor α, is given by:

$$I^{p}_{ii'} \propto \left(\frac{\partial \alpha_{ii'}}{\partial Q_p} \right)^2. \tag{2}$$

The relative Raman intensities of the peaks are computed analytically by exploiting a scheme, implemented in the CRYSTAL program,[31,32] which constitutes an extension of the analytical calculation of IR intensities.[32,33] Both schemes are based on the solutions of first- and second-order Coupled–Perturbed–Hartree–Fock/Kohn–Sham (CPHF/KS) equations.[60,61] The Raman spectrum is then computed by considering the transverse-optical (TO) modes and by adopting a pseudo-Voigt functional form consisting of Lorentzian curve with full width at half maximum of 8 cm^{-1}. Raman intensities are normalized so that the highest value is conventionally set to 1000 a.u. Integrated intensities for IR absorption $\mathscr{I}_p$ are computed for each mode p by means of the mass-weighted effective-mode Born-charge vector $\vec{Z}_p$[62,63] evaluated through a CPHF/KS approach.[32,33]

3 Results

3.1 Geometries, spin charges distribution and band structure

The top left panel of Fig. 1 shows the conventional diamond lattice, in which the generic split interstitial is created. The two atoms involved in the defect (A and B, in green) can be either one carbon and one nitrogen (I_{1N}), both nitrogens (I_{2N}) or both carbons (I_{2C}). As mentioned earlier, the latter defect, widely known as 〈100〉 split self-interstitial, has been the subject of a previous investigation,[38] and is included here for the purposes of comparison. In panels a, b, and c of Fig. 1 equilibrium geometries of the I_{1N}, I_{2N} and I_{2C} point defects in diamond are reported. Also shown in Fig. 1 are the corresponding net atomic charge, spin and overlap bond populations, OBP, (all in |*e*|) derived from Mulliken partitioning of the electron density.

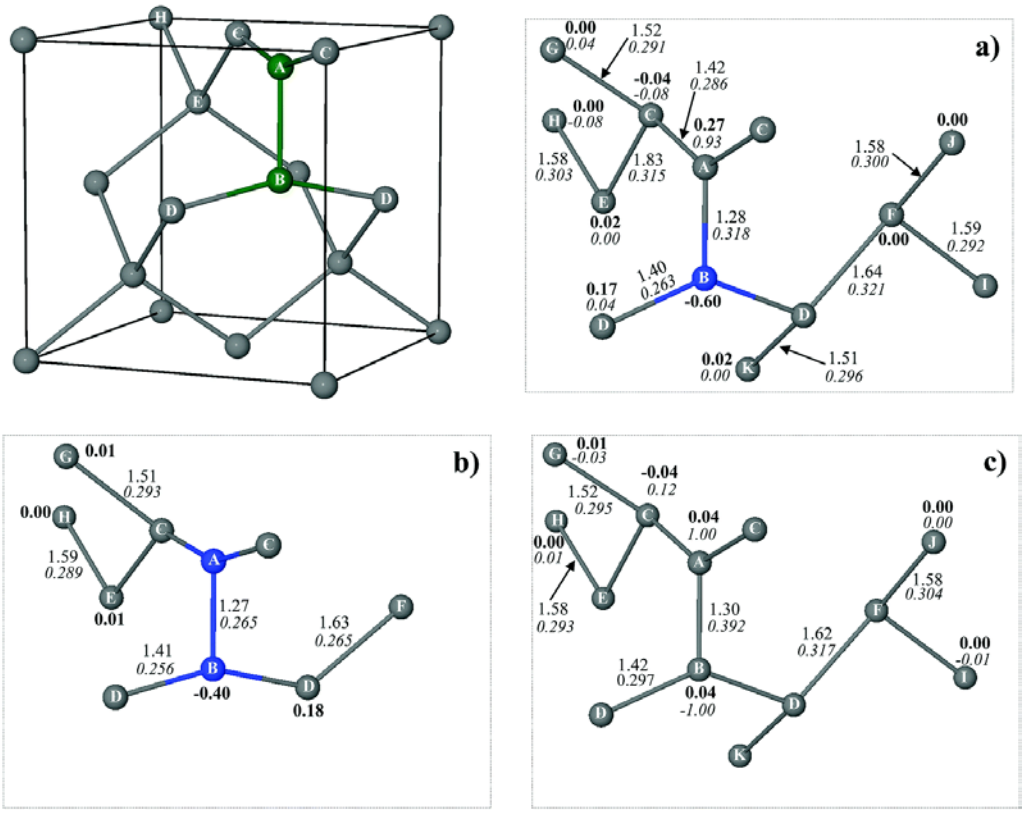

Fig. 1 Schematic representation of the 〈100〉-split interstitial, where the two atoms forming the defect (A and B) are reported in green. These can be either one C and one N (panel a, I_{1N}), both N (panel b, I_{2N}), or both C (panel c, I_{2C}). B3LYP Mulliken net (|*e*|, in bold) and spin charges (|*e*|, in italic) are reported for each atom displayed. Bond lengths (in Å) and Mulliken bond population (|*e*|, in italic) are also reported.

From a structural point of view the differences between the I_{2C} defect and the two containing nitrogen (I_{1N} and I_{2N}) are, as expected, rather small, for carbon and nitrogen are neighbouring elements in the Periodic Table and their covalent radii, 73 and 71 pm,[64] are comparable. One of the few noteworthy differences between I_{2C} and both I_{1N} and I_{2N} is the bond length between atoms A and B, which decreases slightly as the number of nitrogen increases, from 1.30 Å for I_{2C} to 1.27 Å for I_{2N}. Fig. 1 also shows that, concomitant with these changes in bond length, there are corresponding changes in the Mulliken charge and spin populations.

In the I_{2C} defect (Fig. 1c), where only carbons are present, remarkably, no net local charges are found. For the I_{1N} defect (Fig. 1a), on the other hand, the difference in electronegativity between nitrogen and its neighbours polarises the electron density, leading to a net charge of −0.60 |*e*| on the impurity and net charges of +0.27 |*e*| and +0.17 |*e*| on atoms A and D respectively. In the case of I_{2N}, both nitrogens have a Mulliken net charge of −0.40 |*e*|, which is almost completely neutralised by charges of +0.18 |*e*| on the 4 neighboring carbon atoms. This perturbation on the electron density due to the presence of nitrogen, however, is very local and its effect, short-range, for, as panel b of Fig. 1 shows, it does not propagate to the second and third neighbours of the defect.

Before considering the details of the electron spin distributions, we note, first, that each of the two carbon atoms of the I_{2C} defect, our reference system, has a single unpaired electron, which is associated with a “dangling bond”, as a result of the three-fold coordination. This leads to two possible spin states, namely, an open-shell, but paired, singlet (S_z = 0) [$C_A(\alpha)C_B(\beta)$] and a triplet (S_z = 1) [$C_A(\alpha)C_B(\alpha)$], of which the former is slightly more stable by 0.027 eV.[38] The very small energy difference is a consequence of the fact that the unpaired electrons populate orthogonal atomic orbitals: they essentially ignore each other. In the case of I_{1N}defect, there is a single unpaired electron associated with the carbon atom, as the three-fold coordination of the nitrogen satisfies its normal valence. This leads to one possible spin state, the doublet (S_z = ½). The spin state of I_{2N} is even simpler, for there are no unpaired electrons, since both nitrogen atoms are three-fold coordinated. This closed-shell configuration is the origin of the EPR inactivity. The above-mentioned spin multiplicities all refer to the ground states of the respective defects.

Fig. 2 compares bi-dimensional spin density maps of the I_{1N} and I_{2C} defects, where the selected orthogonal projection planes are defined by atoms A, B, and C (top panels) and A, B, and D (bottom panels). As can be observed, the single unpaired electron in I_{1N} is almost entirely localized on carbon atom A, conventionally with α-spin, which induces a small β-polarization on its first neighbours to reduce Pauli repulsion. In the case of I_{2C}, the strong localisation of the unpaired electrons on each of the two carbon atoms is clearly evident; note that, despite the availability of two electrons on neighboring atoms, the formation of a double bond is hindered due to geometrical constraints (see discussion in ref. 38; the two unpaired electrons occupy mutually orthogonal orbitals).

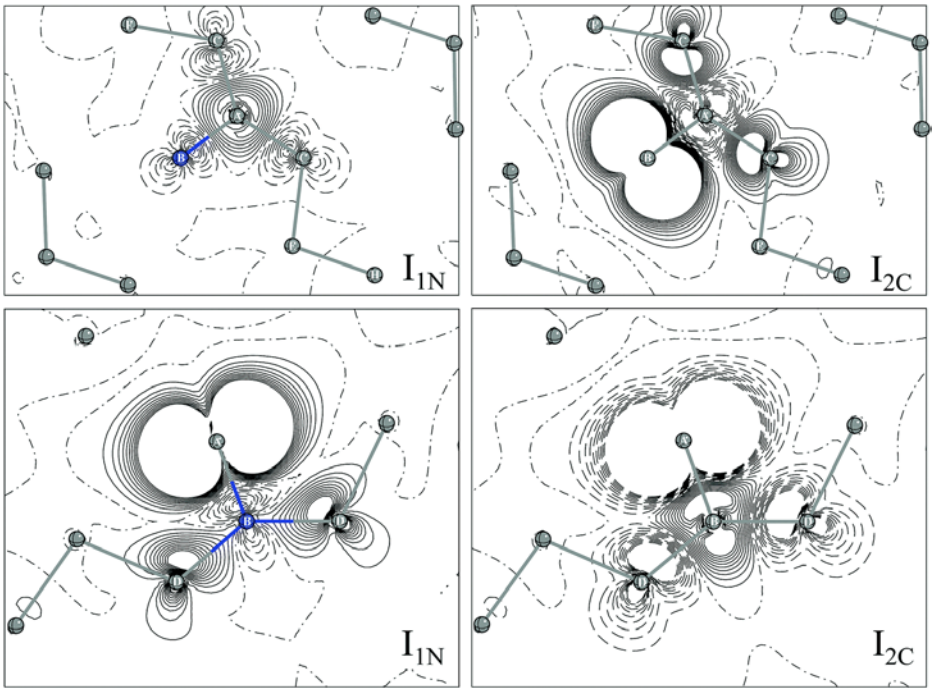

Fig. 2 B3LYP spin density maps of I_{1N} and I_{2C} defects in diamond. Referring to Fig. 1, orthogonal projection planes are defined by atoms A, B, and C (top panels) and A, B, and D (bottom panels). Isodensity lines differ by 0.01 $|e|$ $(a_0)^{-3}$; spin density is truncated at ±0.1 $|e|$ $(a_0)^{-3}$. Continuous, dashed and dot-dashed black lines indicate positive, negative and zero values, respectively.

Fig. 3 compares the band structures of pristine diamond with those of I_{1N}, I_{2N} and I_{2C} based on S_{64} supercells, where the horizontal blue line represents the Fermi level, E_F. Note, however, that in this figure the Fermi level simply provides a convenient demarcation between the occupied and virtual orbitals. The continuous black and red lines indicate α and β spin bands respectively, and for the closed-shell systems, pristine diamond and I_{2N}, the α and β bands are superimposed. A number of interesting and noteworthy features emerge from these. First, the band gaps of the defective systems, 5.59 eV, 5.56 eV and 5.45 eV for I_{1N}, I_{2N} and I_{2C} respectively, are all less than, but within 5% of the perfect diamond value of 5.73 eV. Second, the band structure of the reference I_{2C} defect in its singlet state, contains a pair of occupied, degenerate, spin polarised bands, one α and one β, approximately 1 eV below E_F, containing the two unpaired electrons, and a corresponding pair of unoccupied bands approximately 2 eV above the Fermi level. Third, the totally spin-paired I_{2N} defect contains a pair of doubly-occupied, low-lying nitrogen bands approximately 2 eV below E_F, which are dispersed by less than 0.5 eV and are degenerate at the Γ-point. Fourth, the band structure of I_{1N} is similar to those of I_{2C} and I_{2N}, allowing for the differences in chemical composition and number of unpaired electrons. It contains one similarly-flat, doubly-occupied nitrogen band, approximately 1 eV below the Fermi level (the I_{2N} bands are 2 eV below E_F), one singly-occupied carbon spin band, approximately 2 eV below E_F (the I_{2C} bands are 1 eV below) and one un-occupied carbon spin band approximately 2 eV above the Fermi level, as it is in I_{2C}.

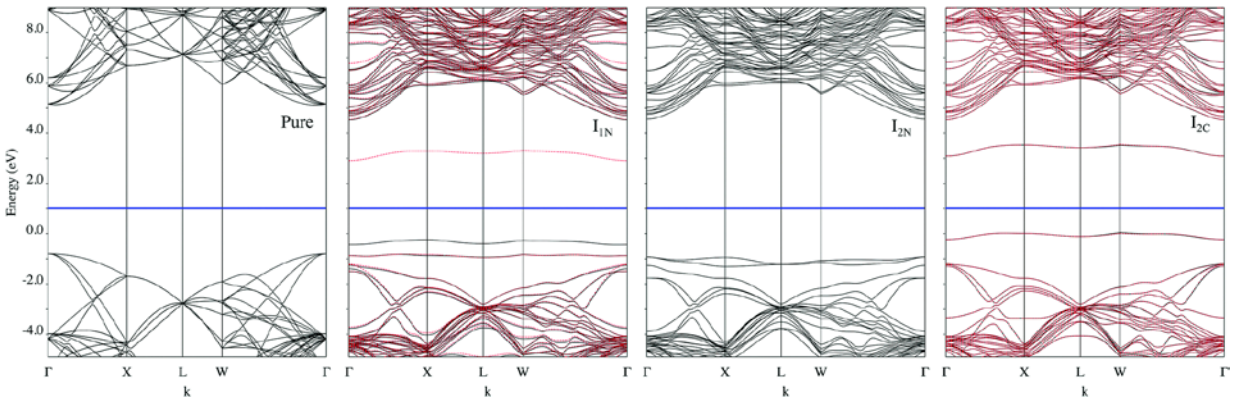

Fig. 3 B3LYP band structure of the pure (first panel) and defective diamond (I_{1N}, I_{2N} and I_{2C} in second, third and fourth panels, respectively). Reported data refer to the S_{64} supercell. Black-continuous and red-dotted lines indicate energy bands accessible for electrons with α and β spins, respectively. Horizontal blue line marks the position of the Fermi energy.

Turning now to the formation energy of these defects, Table 1 reports these for a set of different density functionals. In this paper, formation energies of the I_{1N} and I_{2N} defects have been defined as the total energy difference between "products" and "reactants" of the following reaction:

$$\text{Diamond} + a\cdot\text{N (or C)} \rightarrow \text{I}_{a\text{N}} + (a-1)\cdot\text{C} \qquad (3)$$

where a is the number of nitrogen atoms inserted, while $(a-1)$ is the number of carbons that have been removed. To reduce the Basis Set Superposition Error (BSSE), atomic energies of isolated nitrogen and carbon atoms have been calculated including two shells of neighboring ghost functions. As can be observed, the three hybrid functionals provide rather coherent values of formation energies, which are approximatively 6, 8, and 4.5 eV for the I_{1N}, I_{2N} and I_{2C}, respectively. The PBE and LDA functionals, which contain no exact Hartree–Fock exchange, lead to underestimates of the formation energies compared with the B3LYP values, that range from 1.0 eV (I_{2N}) to 0.83 eV (I_{1N}) for PBE, and from 1.88 eV (I_{2N}) to 1.57 eV (I_{2C}) for LDA.

Table 1 Formation energies of the I_{1N}, I_{2N} and I_{2C} point defects in diamond. Values, in eV, refer to the S_{64}supercell and are obtained according to eqn (3)

Method	**I_{1N}**	**I_{2N}**	**I_{2C}**
B3LYP	5.96	7.88	4.69
PBE0	5.97	8.14	4.45
HSE06	5.97	8.13	4.44
PBE	5.14	7.14	3.73
LDA	4.28	6.04	3.12

3.2 Infrared and Raman spectra

Vibrational spectroscopy makes a significant contribution to the identification of the different types of defect present in diamond. Now it is generally rather difficult to assign a given spectral feature unambiguously to a specific structural defect, from experiment alone, since, potentially, there is a large number of factors such as defect type, concentration, aggregation *etc.*, that might hinder or complicate this. However, the same is not true for simulations, since the nature of a particular defect, its concentration and local environment *i.e.*, bulk, surface grain boundary, presence of impurity *etc.*, can be defined exactly *a priori*.

The experimental Raman spectrum of pristine diamond is simple, for it consists of a single and sharp peak at the experimental value of 1332 cm^{-1}, while the IR spectrum is featureless, due to symmetry constraints. For these reasons, all features observed in the simulated IR spectrum can be attributed to the presence of the specific defect(s) contained in the simulation, while all features that appear in the Raman spectrum, aside from the one-phonon mode at 1332 cm^{-1} can similarly be assigned. Among the many peaks that appear in simulated spectra of defective diamond, those that appear above 1332 cm^{-1} are of particular interest, for these can be related to vibrational normal modes that involve the displacements of just a few sets of atoms, typically those of the defect and their nearest neighbors.

As with all quantum mechanically-based studies of the type reported in this paper, the accuracy and dependability of the results are determined, in large measure, by the quality of the basis set used. However, for calculations of the size used in the present study, which involve the direct structural minimisation of defective cells containing up to 216 atoms, inevitably a balance needs to be struck between basis set size, accuracy and computational cost. Here a modified Pople 6-21G basis set has been chosen, which, we believe achieves this balance. To illustrate this, Table 2, lists the calculated zero-phonon Raman frequencies for perfect diamond derived from 6-21G, 6-21G*, 6-31G and 6-31G* basis sets compared with estimates of the computation times for the structural minimisation of defective cells containing 216 atoms. Thus, a reduction in the error of the computed Raman frequency, compared with the experimental frequency of 1332 cm^{-1}, from 1.1% for 6-21G to 0.5% for 6-21G* requires 1.16 times the computational cost, while a further reduction to 0.3% for 6-31G requires 1.75 times the cost. Importantly, the 6-31G* basis set is 4.5 times more costly, with an increased error of 1.6%.

Table 2 Comparison of the predicted zero-phonon Raman frequency, $\bar{\nu}$ (cm^{-1}), deviation from the experimental value of 1332 cm^{-1}, Δ (%), and relative computation cost, *S*, for different basis sets

Basis set	$\bar{\nu}$	Δ **(%)**	***S***
6-21G	1317.0	−1.1	1.00
6-21G*	1325.9	−0.5	1.16
6-31G	1336.4	+0.3	1.76
6-31G*	1353.8	+1.6	4.50

3.3 Infrared spectrum

Starting with the IR spectrum of the reference defect, I_{2C}, shown in the right-hand panels of Fig. 4, an animation of the normal modes (available at www.crystal.unito.it) indicates that the peak at 1519 cm^{-1} (1506 cm^{-1} from S_{64}) corresponds to a doubly-degenerate (*E* symmetry) asymmetric C–C stretch involving atoms labelled C–A–C and D–B–D in Fig. 1c. This indicates that the frequency is determined solely by the nature of the three atoms, in this case all six are carbon, and is apparently unaffected by the coordination of atoms C and D, which are different. Visual analysis shows that the two modes at 448 cm^{-1} and 561 cm^{-1} correspond to 'waggling' modes of the self-interstitial, again associated with C–A–C and D–B–D. At the higher defect concentration (S_{64}), the lower frequency line is shifted upwards by 5 cm^{-1}, while the intensity of the higher frequency line is substantially reduced to the point where it is barely discernible.

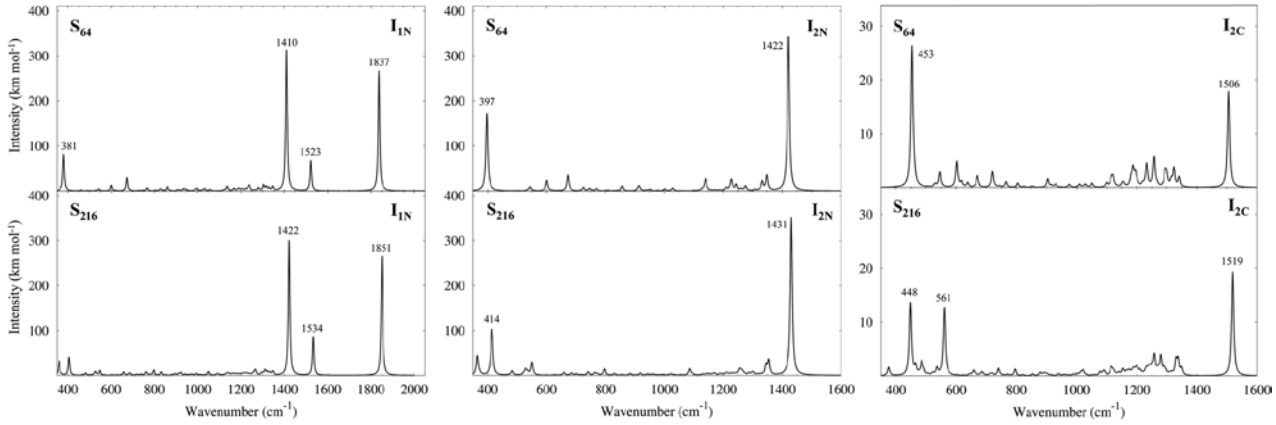

Fig. 4 B3LYP simulated IR spectra of the I_{1N}, I_{2N} and I_{2C} defects in diamond for both S_{64} and S_{216} supercells (top and bottom panels, respectively).

Turning now to I_{2N}, which has a similar (local) D_{2d} symmetry as the reference defect, the middle panels of Fig. 4show that there is a similar, high-frequency doubly-degenerate asymmetric stretch of N–N, now at 1431 cm^{-1}, with a shift of −9 cm^{-1} at the higher defect concentration (S_{64}). Once again, visual inspection indicates that these stretching modes involve the neighbouring atoms C and D. There is a similar 'waggling' mode at 414 cm^{-1}(448 cm^{-1} in I_{2C}), which is shifted by −17 cm^{-1} at the higher defect concentration, with a slight increase in intensity. Overall, the spectra of these two symmetric ⟨100⟩ split interstitials are very similar, with differences that can straightforwardly be attributed to the differences in chemical composition.

The IR spectrum of I_{1N}, shown in the left-hand panels of Fig. 4, is richer than those of I_{2N} and I_{2C}, in that it contains three new features above the one-phonon mode, at 1422 cm^{-1}, 1534 cm^{-1} and 1851 cm^{-1}, with reductions of ∼12 cm^{-1}, but comparable intensities, for S_{64} cells. Vibrational animation shows that the two lower frequency peaks correspond to the I_{2N} and I_{2C} features at 1431 cm^{-1} and 1519 cm^{-1} respectively, with the 1422 cm^{-1} mode assigned to the B_1 asymmetric C–N–C stretch, and the 1534 cm^{-1} mode to the B_2 asymmetric C–C–C stretch (C in the last two mode designations refers to carbon atoms, and not the labels of Fig. 1). It is of interest to note that the frequency (energy) of the asymmetric C–N–C stretch in

I_{1N} is less than it is in I_{2N}, whereas the frequency of the corresponding C–C–C stretch in I_{1N} is greater than that in I_{2C}. Again, visual inspection assigns the 1851 cm^{-1} feature to the symmetric C–N stretch of the two interstitial atoms. This mode is not observed in the spectra of I_{2N} or I_{2C}, for these have local D_{2d} symmetry, the breaking of which by the dissimilar neighbouring carbon pairs (C_2 and D_2 of Fig. 1) is unable to induce a sufficiently large dipole moment for measurable intensity. Finally, the S_{64} 'waggling' mode in I_{2N} and I_{2C} at 397 cm^{-1} and 453 cm^{-1} respectively, is seen at 381 cm^{-1}; but there is no measurable intensity for this mode at the lower defect concentration.

However, it is worth mentioning that while defect-induced spectral features above the pristine diamond first-order peak can be readily detected from experiment, this is not the case for the spectral region below the one-phonon absorption band. This is due to the fact that any defect-induced reduction of symmetry in diamond generates a broad band in the region between 300 and 1300 cm^{-1}, which is essentially proportional to the vibrational density of states.

3.4 Raman spectrum

The simulated Raman spectra of the I_{1N}, I_{2N} and I_{2C} defects for the S_{64} (top panels) and S_{216} (bottom panels) supercells are reported in Fig. 5, where the intense one-phonon peak of the perfect diamond lattice at 1317 cm^{-1}, is again prominent, but slightly shifted, to 1331 cm^{-1}, 1333 cm^{-1} and 1324 cm^{-1} respectively, separating the spectra into two regions. The one below the first-order Raman peak is rather complex and with many close peaks, that are usually associated with collective-normal modes; the region above the pristine diamond Raman feature shows, instead, rather distinct spectroscopic features, which are commonly related to localized vibrational modes.

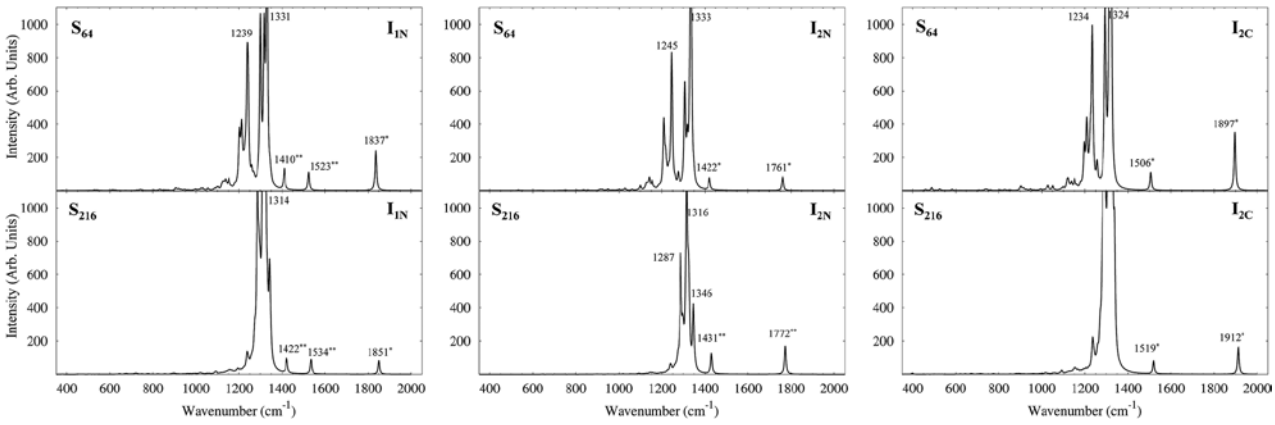

Fig. 5 B3LYP simulated Raman spectra of the I_{1N}, I_{2N} and I_{2C} defects in diamond for both S_{64} and S_{216} supercells (top and bottom panels, respectively). Intensity of the peaks marked by (*) and (**) have been multiplied by 10 and 100, respectively.

Turning now to a more detailed analysis, the principle features in the IR spectra reported in the previous section should also be found in the Raman spectra, albeit possibly with minor adjustments resulting from the interaction with nearby modes that are not found in the former spectra. As reported previously,[38] the Raman spectrum of I_{2C} contains three active modes above the first-order frequency, two degenerate asymmetric stretching modes at 1519 cm^{-1} and a symmetric mode at 1912 cm^{-1} (1506 cm^{-1} and 1897 cm^{-1} from S_{64}).

The Raman spectrum of I_{2N} is similar to that of I_{2C}, though shifted to lower frequency by ~7% and ~10% with the intensity, with asymmetric and symmetric stretches at 1431 cm^{-1} and 1772 cm^{-1} respectively (1422 cm^{-1} and 1761 cm^{-1} from S_{64}). Predictably, the Raman spectrum of I_{1N} is richer than those of I_{2N} and I_{2C}, but, as before, broadly in line with the IR spectrum. The frequency of the symmetric stretch, 1851 cm^{-1} (1837 cm^{-1} from S_{64}), is identical to the IR frequency, and compares with values of 1772 cm^{-1} and 1912 cm^{-1} for I_{2N} and I_{2C} respectively. The changes in frequency of +79 cm^{-1} and −61 cm^{-1} from those in I_{2N} and I_{2C} suggest that the interstitial bond strengths in diamond are in the order C–C > C–N > N–N, which compares with C=C ≈ C=N > N=N in molecules (https://chem.libretexts.org >…> Fundamentals of Chemical Bonding).

4 Discussion

The prime motivation of this study, as on previous occasions,[25–30] is to show that all-electron quantum mechanical calculations based on the CRYSTAL code[37] can provide detailed, quantitative IR and Raman spectra for the common defects in diamond. The utility of this approach is predicated on the twin facts that perfect, or pristine diamond exhibits no IR features, for symmetry reasons, and that the Raman spectrum consists of a single, sharp one-phonon peak at 1332 cm^{-1}, which compares with the calculated B3LYP/6-21G value of 1317 cm^{-1}.[25–30] It follows, therefore, that all IR features exhibited by real crystals, and all Raman features other than the sharp one-phonon peak, are due to the presence of defects. However, real crystals contain a multitude of defects, mostly of unknown provenance, so that the assignment of spectral features to individual defects is both difficult and uncertain. On the other hand, calculations can be performed for completely defined defects at specific concentrations, from which the unambiguous assignment of spectral features is readily available.

Following previous studies,[25–30] this paper reports the IR and Raman spectra of the ⟨100⟩ split-interstitial defects, I_{2C}, I_{2N} and I_{1N}, obtained from all-electron Gaussian orbital B3LYP calculations based on periodic 64- and 216-atom supercells (S_{64} and S_{216}) using the CRYSTAL computer code.[37] The principal feature of both types of spectra is the presence of well-defined peaks above the one-phonon Raman frequency, which recently-developed visualisation techniques (www.crystal.unito.it) are able to assign with minimum ambiguity. These features consist the symmetric stretch of the interstitial pair, and doubly degenerate asymmetric stretches corresponding to atoms C–A–C and D–B–D, in the notation of Fig. 1, where A and B are carbon and nitrogen atoms according to the defect, and C and D, inequivalent lattice carbon atoms. As expected, the symmetric stretches are seen in the Raman spectra of the three defects, whereas it is only for I_{1N} that this mode is seen in the IR spectrum. The asymmetric stretches for the three defects are seen in both the IR and Raman spectra. In all cases, there is a shift to lower frequency by about 1% on increasing the defect concentration from the S_{216} to the S_{64} simulations. This suggests that for real crystals, where the defect concentrations are generally much lower than those considered here, the S_{216} frequencies in particular, might reasonably be considered as (quantitative) predictions, in view of the fact that the calculated one-phonon Raman frequency is within 1% of the measured value.

Finally, it is interesting to compare the wavenumbers reported in this work with those provided by Goss and coworkers,[39] where calculations on S_{64} and S_{216} supercells have performed with local spin density functional and pseudopotentials. As regards the I_{1N} point defect, our values of 1422, 1534 and 1851 cm^{-1} for asymmetric and symmetric stretches compare with those of 1461, 1537 and 1861 cm^{-1},

respectvely: while for I_{2N}, our values of 1431 and 1772 cm^{-1} values compare with 1454 and 1830 cm^{-1}, reported previously.[39]

5 Conclusion

The principal conclusion of this paper is that the three interstitial defects in diamond, I_{2C}, I_{2N} and I_{1N}, are predicted to have measurably different IR and Raman signatures from each other, and from pristine diamond. The particular significance of the latter is that the present results make an important contribution to the analysis and characterisation of the spectra of both natural and synthetic diamonds. There are no previous reports, either of the frequencies or relative intensities of these novel spectral features based on full quantum mechanical methodology. Specifically, this study predicts that in addition to the presence of relatively low intensity collective modes in the region of the one-phonon Raman frequency, the ⟨100⟩ split-interstitial defects, I_{2C}, I_{2N} and I_{1N}give rise to doubly-degenerate asymmetric stretching modes which are both IR and Raman active for all three defects, and a higher frequency symmetric stretch which again is Raman active for the three interstitials, but is IR active only for I_{1N}. The frequencies of this mode suggest that the split-interstitial bond strengths in diamond are in the order C–C > C–N > N–N, which is supported by the calculated Mulliken bond populations (0.392, 0.318 and 0.265 $|e|$, respectively).

Conflicts of interest

There are no conflicts to declare.

Acknowledgements

SS and RD acknowledge the Cineca award (HP10CLF46D) under the Iscra initiative, for the availability of high performance computing resources and support. Some of the present calculations were performed by FP using HPC resources from GENCI-[CINES/IDRIS/TGCC] (Grant 2018-[A0040810471]).

References

1. S. J. Breuer and P. R. Briddon, Ab Initio Investigation of the Native Defects in Diamond and Self-Diffusion, Phys. Rev. B: Condens. Matter Mater. Phys., 1995, 51(11), 6984–6994.
2. A. Mainwood, Modelling of Interstitial-Related Defects in Diamond, Diamond Relat. Mater., 1999, 8(8), 1560–1564.
3. R. Kalish, A. Reznik, S. Prawer, D. Saada and J. Adler, Ion-Implantation-Induced Defects in Diamond and Their Annealing: Experiment and Simulation, Phys. Status Solidi A, 1999, 174(1), 83–99.
4. G. Davies, B. Campbell, A. Mainwood, M. Newton, M. Watkins, H. Kanda and T. R. Anthony, Interstitials, Vacancies and Impurities in Diamond, Phys. Status Solidi A, 2001, 186(2), 187–198.
5. J. P. Goss, R. Jones, T. D. Shaw, M. J. Rayson and P. R. Briddon, First Principles Study of the Self-Interstitial Defect in Diamond, Phys. Status Solidi A, 2001, 186(2), 215–220.
6. G. Davies, H. Smith and H. Kanda, Self-Interstitial in Diamond, Phys. Rev. B: Condens. Matter Mater. Phys., 2000, 62, 1528–1531.
7. D. J. Twitchen, D. C. Hunt, M. E. Newton, J. M. Baker, T. R. Anthony and W. F. Banholzer, Electron Paramagnetic Resonance (EPR) and Optical Absorption Studies of Defects Created in Diamond by Electron Irradiation Damage at 100 and 350 K, Phys. B, 1999, 273, 628–631.
8. P. F. Lai, S. Prawer and C. Noble, Electron Spin Resonance Investigation of Ion-Irradiated Diamond, Diamond Relat. Mater., 2002, 11(7), 1391–1396.
9. A. Moroño, S. M. González de Vicente and E. R. Hodgson, Radiation Effects on the Optical and Electrical Properties of CVD Diamond, Fusion Eng. Des., 2007, 82(15), 2563–2566.
10. A. C. Ferrari and J. Robertson, Interpretation of Raman Spectra of Disordered and Amorphous Carbon, Phys. Rev. B: Condens. Matter Mater. Phys., 2000, 61, 14095–14107.
11. A. C. Ferrari and J. Robertson, Resonant Raman Spectroscopy of Disordered, Amorphous, and Diamondlike Carbon, Phys. Rev. B: Condens. Matter Mater. Phys., 2001, 64, 075414.
12. R. Kalish, A. Reznik, K. W. Nugent and S. Prawer, The Nature of Damage in Ion-Implanted and Annealed Diamond, Nucl. Instrum. Methods Phys. Res., Sect. B, 1999, 148(1), 626–633.
13. H. Amekura and N. Kishimoto, Effects of High-Fluence Ion Implantation on Colorless Diamond Self-Standing Films, J. Appl. Phys., 2008, 104(6), 63509.
14. D. N. Jamieson, S. Prawer, K. W. Nugent and S. P. Dooley, Cross-sectional Raman Microscopy of MeV Implanted Diamond, Phys. Rev. B: Condens. Matter Mater. Phys., 1995, 106, 641–645.
15. J. D. Hunn, S. P. Withrow, C. W. White and D. M. Hembree Jr, Raman Scattering from MeV-Implanted Diamond, Phys. Rev. B: Condens. Matter Mater. Phys., 1995, 52, 8106–8111.
16. S. Prawer, K. W. Nugent and D. N. Jamieson, The Raman Spectrum of Amorphous Diamond, Diamond Relat. Mater., 1998, 7, 106–110.
17. J. O. Orwa, K. W. Nugent, D. N. Jamieson and S. Prawer, Raman Investigation of Damage Caused by Deep Ion Implantation in Diamond, Phys. Rev. B: Condens. Matter Mater. Phys., 2000, 62(9), 5461–5472.
18. R. Brunetto, G. A. Baratta and G. Strazzulla, Raman Spectroscopy of Ion Irradiated Diamond, J. Appl. Phys., 2004, 96, 380–386.
19. P. Olivero, S. Rubanov, P. Reichart, B. C. Gibson, S. T. Huntington, J. R. Rabeau, A. D. Greentree, J. Salzman, D. Moore, D. N. Jamieson and S. Prawer, Characterization of Three-

Dimensional Microstructures in Single-Crystal Diamond, Diamond Relat. Mater., 2006, 15, 1614–1621.

20. S. Prawer, I. Rosenblum, J. O. Orwa and J. Adler, Identification of the Point Defects in Diamond as Measured by Raman Spectroscopy: Comparison Between Experiment and Computation, Chem. Phys. Lett., 2004, 390, 458–461.
21. A. A. Bergman, A. M. Zaitsev, M. Huang and A. A. Gorokhovsky, Photoluminescence and Raman Studies of Xe Ion-Implanted Diamonds: Dependence on Implantation Dose, J. Lumin., 2009, 129, 1524–1526.
22. J. P. Goss, B. J. Coomer, R. Jones, C. J. Fall, P. R. Briddon and S. Öberg, Extended Defects in Diamond: The Interstitial Platelet, Phys. Rev. B: Condens. Matter Mater. Phys., 2003, 67, 165208.
23. J. P. Goss, B. J. Coomer, R. Jones, T. D. Shaw, P. R. Briddon, M. Rayson and S. Öberg, Self-Interstitial Aggregation in Diamond, Phys. Rev. B: Condens. Matter Mater. Phys., 2001, 63(19), 195208.
24. D. Hyde-Volpe, B. Slepetz and M. Kertesz, The [V–CC–V] Divacancy and the Interstitial Defect in Diamond: Vibrational Properties, J. Phys. Chem., 2010, 114(21), 9563–9567.
25. S. Salustro, G. Sansone, C. M. Zicovich-Wilson, Y. Noël, L. Maschio and R. Dovesi, The A-center Defect in Diamond. A Quantum Mechanical Characterization Through the Infrared Spectrum, Phys. Chem. Chem. Phys., 2017, 19, 14478–14485.
26. S. Salustro, A. M. Ferrari, F. S. Gentile, J. K. Desmarais, M. Rérat and R. Dovesi, Characterization of the B-center Defect in Diamond Through the Vibrational Spectrum. A Quantum Mechanical Approach, J. Phys. Chem. A, 2018, 122(2), 594–600.
27. F. Gentile, S. Salustro, M. Causá, A. Erba, P. Carbonniére and R. Dovesi, The VN_3H Defect in Diamond. A Quantum Mechanical Investigation of the Structural, Electronic and Vibrational Properties, Phys. Chem. Chem. Phys., 2017, 1(4), 1–2.
28. S. Salustro, F. S. Gentile, P. D'Arco, B. Civalleri, M. Rérat and R. Dovesi, Hydrogen Atoms in the Diamond Vacancy Defect. A Quantum Mechanical Vibrational Analysis, Carbon, 2018, 129, 349–356.
29. G. Sansone, S. Salustro, Y. Noël, L. Maschio, W. C. Mackrodt and R. Dovesi, Looking for sp^2 Carbon Atoms in Diamond: a Quantum Mechanical Study of Interacting Vacancies, Theor. Chem. Acc., 2018, 137(2), 29.
30. S. Salustro, F. S. Gentile, A. Erba, P. Carbonniére, K. El-Kelany and R. Dovesi., The Characterization of the VN_xH_y Defects in Diamond through the Infrared Vibrational Spectrum. A Quantum Mechanical Investigation, Carbon, 2018, 132, 210–219.
31. L. Maschio, B. Kirtman, R. Orlando and M. Rérat, Ab Initio Analytical Infrared Intensities for Periodic Systems Through a Coupled Perturbed Hartree–Fock/Kohn–Sham Method, J. Chem. Phys., 2012, 137(20), 204113.
32. L. Maschio, B. Kirtman, M. Rérat, R. Orlando and R. Dovesi, Ab Initio Analytical Raman Intensities for Periodic Systems Through a Coupled Perturbed Hartree–Fock/Kohn–Sham Method in an Atomic Orbital Basis. II. Validation and Comparison with Experiments, J. Chem. Phys., 2013, 139(16), 164102.
33. L. Maschio, B. Kirtman, M. Rérat, R. Orlando and R. Dovesi, Comment on “Ab Initio Analytical Infrared Intensities for Periodic Systems Through a Coupled Perturbed Hartree–Fock/Kohn–Sham Method”, J. Chem. Phys., 2013, 139, 167101 (J. Chem. Phys. , 2012 , 137, 204113).

34. C. Carteret, M. De La Pierre, M. Dossot, F. Pascale, A. Erba and R. Dovesi, The Vibrational Spectrum of $CaCO_3$ Aragonite: a Combined Experimental and Quantum-Mechanical Investigation, J. Chem. Phys., 2013, 138(1), 014201.
35. L. Maschio, B. Kirtman, S. Salustro, C. M. Zicovich-Wilson, R. Orlando and R. Dovesi, Raman Spectrum of Pyrope Garnet. A Quantum Mechanical Simulation of Frequencies, Intensities, and Isotope Shifts, J. Phys. Chem. A, 2013, 117(45), 11464–11471.
36. M. Prencipe, L. Maschio, B. Kirtman, S. Salustro, A. Erba and R. Dovesi, Raman Spectrum of $NaAlSi_2O_6$ Jadeite. A Quantum Mechanical Simulation, J. Raman Spectrosc., 2014, 45, 703–709.
37. R. Dovesi, A. Erba, R. Orlando, C. M. Zicovich-Wilson, B. Civalleri, L. Maschio, M. Rérat, S. Casassa, J. Baima, S. Salustro and B. Kirtman, Quantum-Mechanical Condensed Matter Simulations with CRYSTAL, WIREs, 2018.
38. S. Salustro, A. Erba, C. M. Zicovich-Wilson, Y. Nöel, L. Maschio and R. Dovesi, Infrared and Raman Spectroscopic Features of the Self-Interstitial Defect in Diamond from Exact-Exchange Hybrid DFT Calculations, Phys. Chem. Chem. Phys., 2016, 120, 21288–21295.
39. J. P. Goss, P. R. Briddon, S. Papagiannidis and R. Jones, Interstitial Nitrogen and its Complexes in Diamond, Phys. Rev. B: Condens. Matter Mater. Phys., 2004, 70, 235208.
40. P. Dirac, A Theory of Electrons and Protons, Proc. R. Soc. A, 1930, 126(801), 360–365.
41. A. D. Becke, Density-Functional Thermochemistry. III. The Role of Exact Exchange, J. Chem. Phys., 1993, 98(7), 5648–5652.
42. C. Lee, W. Yang and R. Parr, Development of the Colle–Salvetti Correlation-Energy Formula Into a Functional of the Electron Density, Phys. Rev. B: Condens. Matter Mater. Phys., 1988, 37(2), 785–789.
43. L. Bjaalie, A. Janotti, K. Krishnaswamy and C. G. Van de Walle, Point Defects, Impurities, and Small Hole Polarons in $GdTiO_3$, Phys. Rev. B, 2016, 93, 115316.
44. M. Gerosa, C. Di Valentin, C. E. Bottani, G. Onida and G. Pacchioni, Communication: Hole Localization in Al-Doped Quartz SiO_2 within Ab Initio Hybrid-Functional DFT, J. Chem. Phys., 2015, 143(11), 111103.
45. M. Gerosa, C. E. Bottani, L. Caramella, G. Onida, C. Di Valentin and G. Pacchioni, Defect Calculations in Semiconductors Through a Dielectric-Dependent Hybrid DFT Functional: the Case of Oxygen Vacancies in Metal Oxides, J. Chem. Phys., 2015, 143(13), 134702.
46. I. P. R. de Moreira and R. Dovesi, Periodic Approach to the Electronic Structure and Magnetic Coupling in $KCuF_3$, K_2CuF_4, and $Sr_2CuO_2Cl_2$ Low-Dimensional Magnetic Systems, Int. J. Quantum Chem., 2004, 99(5), 805–823.
47. D. Munoz, N. M. Harrison and F. Illas, Electronic and Magnetic Structure of $LaMnO_3$ from Hybrid Periodic Density-Functional Theory, Phys. Rev. B: Condens. Matter Mater. Phys., 2004, 69(8), 085115.
48. J. C. Wojdeł, I. P. R. de Moreira, S. T. Bromley and F. Illas, On the Prediction of the Crystal and Electronic Structure of Mixed-Valence Materials by Periodic Density Functional Calculations: the Case of Prussian Blue, J. Chem. Phys., 2008, 128(4), 044713.
49. J. P. Perdew, K. Burke and M. Ernzerhof, Generalized Gradient Approximation Made Simple, Phys. Rev. Lett., 1996, 77(18), 3865–3868.
50. C. Adamo and V. Barone, Toward Chemical Accuracy in the Computation of NMR Shieldings: the PBE0 Model, Chem. Phys. Lett., 1998, 298(1), 113–119.
51. A. V. Krukau, O. A. Vydrov, A. F. Izmaylov and G. E. Scuseria, Influence of the Exchange Screening Parameter on the Performance of Screened Hybrid Functionals, J. Chem. Phys., 2006, 125(22), 224106.

52. J. S. Binkley, J. A. Pople and W. J. Hehre, Self-Consistent Molecular Orbital Methods. 21. Small Split-Valence Basis Sets for First-Row Elements, J. Am. Chem. Soc., 1980, 102(3), 939–947.
53. A. D. Becke, A Multicenter Numerical Integration Scheme for Polyatomic Molecules, J. Chem. Phys., 1988, 88(4), 2547–2553.
54. R. Dovesi, V. R. Saunders, C. Roetti, R. Orlando, C. M. Zicovich-Wilson, F. Pascale, B. Civalleri, K. Doll, N. M. Harrison, I. J. Bush, Ph. D'Arco and M. Llunell, CRYSTAL 2014 User's Manual, University of Torino, Torino, 2013.
55. H. J. Monkhorst and J. D. Pack, Special Points for Brillouin-Zone Integrations, Phys. Rev. B: Solid State, 1976, 13(12), 5188.
56. F. Pascale, C. M. Zicovich-Wilson, F. Lòpez Gejo, B. Civalleri, R. Orlando and R. Dovesi, The Calculation of the Vibrational Frequencies of the Crystalline Compounds and its Implementation in the CRYSTAL Code, J. Comput. Chem., 2004, 25(6), 888–897.
57. C. M. Zicovich-Wilson, F. Pascale, C. Roetti, V. R. Saunders, R. Orlando and R. Dovesi, Calculation of the Vibration Frequencies of α-Quartz: The Effect of Hamiltonian and Basis Set, J. Comput. Chem., 2004, 25(15), 1873–1881.
58. A. Erba, M. Ferrabone, R. Orlando and R. Dovesi, Accurate Dynamical Structure Factors from Ab Initio Lattice Dynamics: the Case of Crystalline Silicon, J. Comput. Chem., 2013, 34, 346–354.
59. J. Baima, M. Ferrabone, R. Orlando, A. Erba and R. Dovesi, Thermodynamics and Phonon Dispersion of Pyrope and Grossular Silicate Garnets from Ab Initio Simulations, Phys. Chem. Miner., 2016, 43, 137–149.
60. M. Ferrero, M. Rérat, R. Orlando and R. Dovesi, The Calculation of Static Polarizabilities of Periodic Compounds. The Implementation in the CRYSTAL Code for 1D, 2D and 3D Systems, J. Comput. Chem., 2008, 29, 1450–1459.
61. M. Ferrero, M. Rérat, R. Orlando and R. Dovesi, Coupled Perturbed Hartree–Fock for Periodic Systems: The role of Symmetry and Related Computational Aspects, J. Chem. Phys., 2008, 128, 014110.
62. G. M. Barrow, Introduction to Molecular Spectroscopy, McGraw-Hill, New York, 1962.
63. B. A. Hess, L. J. Schaad, P. Carsky and R. Zahradnik, Ab Initio Calculations of Vibrational Spectra and Their Use in the Identification of Unusual Molecules, Chem. Rev., 1986, 86, 709–730.
64. J. C. Slater, Atomic Radii in Crystals, J. Chem. Phys., 1964, 41(10), 3199–3204.